



**Size-dependent magnetic and inductive heating properties  
of Fe<sub>3</sub>O<sub>4</sub> nanoparticles: Scaling laws across the  
superparamagnetic size**

Journal:	<i>Physical Chemistry Chemical Physics</i>
Manuscript ID	CP-ART-12-2017-008631.R2
Article Type:	Paper
Date Submitted by the Author:	22-Mar-2018
Complete List of Authors:	Mohapatra, Jeotikanta; University of Texas at Arlington, Department of Physics; University of Texas at Arlington, Zeng, Fanhao; University of Texas at Arlington, Physics Elkins, Kevin; University of TEXAS Arlington, Physics Xing, Meiying; University of Texas at Arlington, Physics Ghimire, Madhav ; University of Memphis Yoon, Sunghyun; Gunsan Natl Univ Mishra, Sanjay; University of Memphis, Physics and Materials Science Liu, J. Ping; University of Texas,

## Size-dependent magnetic and inductive heating properties of Fe<sub>3</sub>O<sub>4</sub> nanoparticles: Scaling laws across the superparamagnetic size

Jeotikanta Mohapatra,<sup>a</sup> Zeng Fanhao,<sup>a</sup> Kevin Elkins,<sup>a</sup> Meiyong Xing,<sup>a</sup> Madhav Ghimire,<sup>b</sup> Sunghyun Yoon,<sup>c</sup> Sanjay R Mishra,<sup>b</sup> J. Ping Liu<sup>a,\*</sup>

<sup>a</sup>*Department of Physics, University of Texas at Arlington, Arlington, TX 76019, USA*

<sup>b</sup>*Department of Physics and Materials Science, The University of Memphis, Memphis, TN, 38152, USA*

<sup>c</sup>*Department of Physics, Gunsan National University, Gunsan, South Korea*

*\*To whom correspondence should be addressed. E-mail: [pliu@uta.edu](mailto:pliu@uta.edu) (J. Ping Liu). Phone: +1-817-272-2815*

### Abstract

An efficient heat activating mediator with an enhanced specific absorption rate (SAR) value is attained via control of the iron oxide (Fe<sub>3</sub>O<sub>4</sub>) nanoparticle size from 3 to 32 nm. The monodispersed Fe<sub>3</sub>O<sub>4</sub> nanoparticles are synthesized *via a seed-less thermolysis* technique using oleylamine and oleic acid as the multifunctionalizing agent (surfactants, solvent and reducing agent). The inductive heating properties as a function of particle size revealed a strong increase in the SAR values with increasing particle size till 28 nm that is above the superparamagnetic size. Particularly, the SAR values of ferromagnetic nanoparticles (> 16 nm) are strongly enhanced with the increase of ac magnetic field amplitude than that for the superparamagnetic (3-16 nm) nanoparticles. The enhanced SAR values in ferromagnetic regime are attributed to the synergistic contribution from the hysteresis and susceptibility loss. Specifically, the 28 nm Fe<sub>3</sub>O<sub>4</sub> nanoparticles exhibit an enhanced SAR value of 801 W/g which is nearly an order higher than that of the commercially available nanoparticles.

## 1. Introduction

Inductive heating in a magnetic fluid is an emerging technology which is currently being discovered for different biomedical applications such as thermal therapy of cancer, thermally activated drug release, remote activation of cell functions, etc.<sup>1-6</sup> In hyperthermia treatment, the magnetic nanoparticle suspension is injected directly into the cancer area that can be heated to 42 - 45 °C by applying an ac magnetic field (ACMF) while maintaining the externally applied field and frequency below the Atkinson- Brezovich limit ( $H \times f \leq 4.85 \times 10^8 \text{ A m}^{-1} \text{ s}^{-1}$ ).<sup>7, 8</sup> This thermotherapy technique has been employed in some clinics as an adjuvant to chemotherapy. In addition, the inductive heating by magnetic nanoparticles (MNPs) is promising for the curing of thermoset resin and also for repairing of potholes on a road.<sup>9</sup> In the latter case, composite of magnetic nanoparticles and asphalt can be filled in the pothole and then irradiated by the ACMF to rebind.<sup>10</sup> However, for most of these applications, relatively poor heating ability of the commercially available nanoparticles (ferumoxytol and feridex) presents a challenging obstacle, which either needs a very strong magnetic field or requires excessively large amounts of nanoparticles.<sup>11</sup> For this purpose, a high efficiency magnetic heating agent is necessitated.

To enhance the heating efficiency, a new class of magnetic nanomaterials may be designed with high saturation magnetization ( $M_S$ ) and moderate effective anisotropy constant ( $K_{eff}$ ).<sup>12</sup> So far, many methods have been adopted to optimize these magnetic parameters to improve the heating property.<sup>13, 14</sup> For example, nanoparticles with hard and soft ferrite core-shell morphology were observed to exhibit improved heating-efficiency attributable to the exchange coupling between the hard core and the soft shell.<sup>15-17</sup> The heating efficiency of iron oxide nanoparticles has also been improved through control of shape.<sup>18-24</sup> <sup>18, 25</sup> Although the anisotropic nanoparticles, nanoparticle nanoassemblies and the core-shell nanoparticles exhibit

higher heating efficiency than the spherical ones, the low yield in the synthesis and the difficulties in controlling the shape anisotropy/core-shell morphology limit their commercialization.

Alternatively, the heating efficiency can be improved in the superparamagnetic to the ferromagnetic transition regime through optimization of hysteresis loss. In general hysteresis loss is determined by  $M_S$  and  $H_C$  and thus much attention has been paid to ferromagnetic nanoparticles with high  $M_S$  and  $H_C$ . A fine tuning of the size of the MNPs can help in improving the hysteresis loss and consequently the heating efficiency. Moreover, the dependence of the SAR on the size of the MNPs is also very complicated. According to the commonly employed linear response theory (Néel and Brownian relaxation), the SAR of the MNPs is supposed to exhibit a maximum around 12 to 15 nm, but this is only valid for small ACMF amplitudes.<sup>26-30</sup> As the ACMF amplitude increases, a more complicated evolution in the trend of the SAR versus MNPs size has been observed. For example, Lv *et al.* have shown experimentally that the SAR reaches a maximum for sizes above 40 nm, while Yamamoto *et al.* and Levy *et al.* observed a maximum for an optimal size of about 12 nm.<sup>19, 26, 30</sup> One of the main problems that restricted a comprehensive comparative size-dependent study of the heating properties of MNPs is the difficulty of synthesizing the monodisperse MNPs in a wide range of sizes. Further, to produce monodispersed nanoparticles above the superparamagnetic size without agglomeration remains to be a technical challenge. To address the challenges, in this study, Fe<sub>3</sub>O<sub>4</sub> nanoparticles with sizes from 3 to 32 nm are synthesized in gram scale quantities *via* thermal decomposition of iron (III) acetylacetonate in oleylamine and oleic acid and then functionalized with citric acid to make them water dispersible. The effects of particle sizes on magnetic and inductive heating properties are systematically studied, in order to understand the heating ability correlation with particle

size. In contrast to the superparamagnetic nanoparticles, the ferromagnetic nanoparticles are in pure magnetite phase, possessing the bulk value of  $M_S$  and most importantly having extremely high SAR values. Moreover, our study established a scaling relationship across the superparamagnetic size of the magnetic and inductive heating properties of  $\text{Fe}_3\text{O}_4$  nanoparticles.

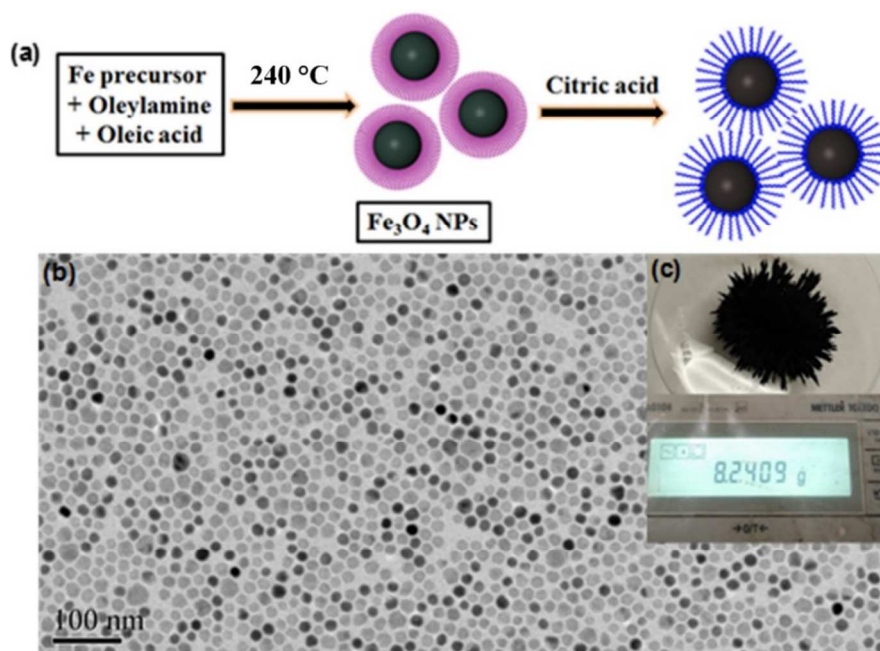
## 2. Experimental Method

### Synthesis of $\text{Fe}_3\text{O}_4$ (2-36 nm) nanoparticles

Monodispersed  $\text{Fe}_3\text{O}_4$  nanoparticles were prepared by a solvent-less thermal decomposition approach. In a typical synthesis of 9 nm  $\text{Fe}_3\text{O}_4$  nanoparticles, 20 mmol of Iron(III) acetylacetonate ( $\text{Fe}(\text{acac})_3$ ) and 60 mmol Oleylamine (OAm) were weighed in a European style three-neck round bottom flask. The reaction solution was dehydrated by sparging forming gas at 100 °C for 30 min in a continuous flow moderated by a gas bubbler. After the dehydration process, the gas flow was stopped and a glass condenser was placed in the center neck of the European-style three-neck flask. The dehydrated reaction solution was then heated to 150 °C under a slight positive pressure of forming gas and remained at this temperature for 15 min. The temperature was elevated to 240 °C later at a heating rate of 5 °C/min for 4 h. The obtained black precipitate was centrifuged and washed with a mixture of hexane and acetone several times to remove organic and inorganic impurities. The size of MNPs was controlled with the variation of  $\text{Fe}(\text{acac})_3$  to OAm mole ratio as 1:3 (9 nm), 1:5 (6 nm), 1:7 (4 nm) and 1:9 (3 nm) respectively. The synthesis procedure of 12-24 nm MNPs was same as the above, except that the oleic acid (OA) was used as an additional surfactant. The modulation of OAm to OA mole ratio 6:1, 6:2 and 6:3 renders 12, 16 and 20 nm  $\text{Fe}_3\text{O}_4$  nanoparticles. To further tune the MNPs size above 20 nm, instead of adding OAm at room temperature, it was injected at 200 °C. In this case,  $\text{Fe}(\text{acac})_3$  and OA mixture was first dehydrated at 100 °C and then heated to 200 °C. Once 200

°C was reached, the required amount of oleylamine was introduced into the reaction medium. The reaction conditions used for the synthesis of MNPs are summarized in Table S1 (ESI). A scale-up experiment was performed using 100 mmol (35 g) of  $\text{Fe}(\text{acac})_3$ , 300 mmol (80 g) of OAm and 100 mmol (28 g) of OA and leading to the formation of nearly 8.2 g of MNPs (~ 16 nm) with a yield of 84%. The percentage yield was calculated after subtraction of the organic contribution (~ 20 %). This confirms that our designed approach can be scaled up without sacrificing the monodispersity. A pictorial illustration of the synthesis procedure is given as schematic view 1.

To use these samples for heat activation study, the as-prepared  $\text{Fe}_3\text{O}_4$  NPs were transferred to an aqueous phase using citric acid. 100 mg of the MNPs was dispersed in 10 ml of toluene and then mixed with 5 mmol of citric acid dissolved in 10 ml of dimethylformamide (DMF). In the forming gas ambience, the MNPs mixture was continuously stirred at 80 °C for 6 h. After the reaction, the citric acid functionalized MNPs were collected by centrifugation and were washed with ethanol several times to remove uncoordinated citric acid molecules.



**Scheme 1:** (a) Schematic representation of citric acid functionalized Fe<sub>3</sub>O<sub>4</sub> nanoparticles. The oleylamine/oleic acid coated Fe<sub>3</sub>O<sub>4</sub> nanoparticles was first synthesized via thermal decomposition of Fe(acac)<sub>3</sub> in OAm and OA at a temperature of 240 °C for 4 h. To make them aqueous dispersible, toluene dispersion Fe<sub>3</sub>O<sub>4</sub> NPs and dimethylformamide (DMF) containing required amount citric acid was heated to 80 °C. (b) TEM micrographs of OA/OAm coated- Fe<sub>3</sub>O<sub>4</sub> nanoparticles confirm that the nanocrystals are uniform in particle-size distribution and of average size 16 nm. Inset is a photograph (Figure c) showing 8.2 g of the Fe<sub>3</sub>O<sub>4</sub> nanoparticles obtained in a single batch.

### Characterization Techniques

X-ray diffraction (XRD) pattern was collected from a Rigaku Ultima IV diffractometer with Cu K- $\alpha$  wavelength (1.5406 Å) X-ray source at a scan rate of 0.12 °/min. High-resolution transmission electron imaging was carried out on Hitachi H-9500 operated at an accelerated voltage of 300 kV. In order to estimate the average MNPs size, the particle size distribution histograms were fitted with either lognormal or Lorentzian distribution function, which was decided based on the  $R^2$  value >0.9. The magnetic properties of the samples were studied using physical property measurement system (Quantum Design Dyanacool-PPMS). The zero-field-cooled (ZFC), and field-cooled (FC) magnetization was measured over the temperature range 10–400 K with an applied field of 50 Oe. The frequency dispersion of the AC susceptibility ( $f = 11, 111, 1111, \text{ and } 9999 \text{ Hz}$ ; amplitude 5 Oe) was measured as a function of temperature. The magnetic hysteresis loop was measured using an Alternating Gradient Magnetometer (AGM) with a magnetic field of 14 kOe. To confirm the oxidation state of Fe in the prepared samples, the room temperature <sup>57</sup>Fe Mössbauer spectroscopy was measured. Mössbauer spectrometer (SEE Co. Minneapolis, MN USA) was calibrated against  $\alpha$ -Fe foil. Fourier transform infrared (FTIR) spectra of the dried powder samples were recorded in the range 400 to 4000 cm<sup>-1</sup> using

FTIR spectrometer (Thermo Nicolet 6700 FTIR Spectrometer). Dynamic light scattering (DLS) and Zeta potential measurements were carried out by using a Zetasizer Nano ZSP (Malvern Instruments, Westborough, Massachusetts) and disposable BRAND® microcuvettes (Sigma-Aldrich). MNPs dispersion (0.1 mg/ml) was measured three times each using five readings per measurement and the resulting data were averaged to obtain a mean size distribution profile and the Zeta potential value for each sample.

The induction heating properties of the aqueous dispersible MNPs were measured using a commercial induction heating system (EASYHEAT 0112). The MNP dispersion of concentration 2 mg/ml was poured into a 5-mL glass vial and kept inside an insulated sample holder positioned at the center of the heating coil. The heating properties were measured at a fixed frequency of 265 kHz, with different field magnitudes of 184, 234, 491 and 625 Oe. The temperature of the water-soluble MNPs was recorded using an alcohol thermometer with accuracy  $\pm 0.5$  °C. Temperature versus time measurements were repeated at least three times with keeping the experimental conditions same and the initial linear slope  $dT/dt$  was obtained by fitting the experimental data at the short time interval. The average SARs along with standard deviation are reported.

### 3. Results and discussion

Over the past years most attention has been paid to synthesize magnetic nanoparticles of desired size and shape. Different synthesis strategies have been found in the literature for obtaining iron oxide nanoparticles with well-defined size/shape and composition.<sup>31-39</sup> However, among them, the high-temperature solution phase method developed by Sun et al appears to be the most interesting because it permits a good control over the size and the morphology of the nanoparticles.<sup>36,37</sup> In this approach, the high-temperature reaction of iron (III) acetylacetonate in

phenyl ether in the presence of 1,2-hexadecanediol, oleic acid, and oleylamine leads formation of  $\text{Fe}_3\text{O}_4$  nanoparticles. In another report, Xu et. al. demonstrated that by varying the heating conditions and ratios of oleylamine and oleic acid, the size of iron oxide nanoparticles can be controlled from 14 to 100 nm.<sup>40</sup> Recently, oleylamine was used as a multitasking agent such as solvent, reducing and surface functionalizing agent to synthesize monodispersed  $\text{Fe}_3\text{O}_4$  nanoparticles with a reasonably large magnetization.<sup>33,41</sup> The experiment shows that the presence of excess amount of oleylamine provides a sufficiently reductive environment for the Fe-precursor and leads formation of  $\text{Fe}_3\text{O}_4$  nanoparticles at a comparatively low temperature of 200 °C. The size of nanoparticles was controlled from 3-9 nm by simple control of the amine to Fe-precursor mole concentration. The  $\text{Fe}_3\text{O}_4$  nanoparticles presented in above mentioned reports are of high quality and the potential of these approaches is that the magnetism can be tuned via precise control of the size and shapes. The above-mentioned studies motivated us to control the oleylamine and oleic acid mole ratio to precisely control the  $\text{Fe}_3\text{O}_4$  nanoparticles sizes over a wide range. Fig. 1 shows TEM micrographs of different sized  $\text{Fe}_3\text{O}_4$  nanoparticles are synthesized by controlling the Fe-precursor to OA and OAm mole ratios. The smaller sized nanoparticles (3-9 nm) are obtained by using OAm as a solvent, surfactant and reducing agent. The decomposition of  $\text{Fe}(\text{acac})_3$  could be due to the presence of the excess amount of OAm which gives a stronger reductive environment for the growth of  $\text{Fe}_3\text{O}_4$  nanoparticles. A systematic variation of  $\text{Fe}(\text{acac})_3$  to OAm mole ratio as 1:3, 1:5, 1:7 and 1:9 provides the MNPs of average sizes 9, 6, 4 and 3 nm, respectively (Fig. 1a-c show the TEM images of 4, 6 and 9 nm MNPs). The continuous decrease of MNPs size with the increase of OAm concentration corroborate the chemisorption of OAm molecules on the MNP surface which restrict the particle growth and ripening process.<sup>42,43</sup> Further to increase the MNPs size above 9 nm, oleic acid was

added to the reaction mixture with keeping the Fe-precursor/amine mole ratio at 1:3. The mole ratio of OAm to OA 6:1, 6:2 and 6:3 renders ~12, ~16 and ~20 nm Fe<sub>3</sub>O<sub>4</sub> nanoparticles. When the mole ratio of OAm to OA is changed to 6:5, anisotropic nanoparticles and low yield were observed (ESI, Fig. S1a). A further increase of oleic acid concentration resulted in a viscous red-brown product (ESI, Fig. S1b). Based on the above experiments and TEM analysis, we proposed a possible growth mechanism of the MNPs synthesis using a bi-surfactant (OAm and OA). We believe the presence of excess amount of oleylamine enhances the deprotonation of oleic acid and leads formation of an acid-amine complex pairs.<sup>44, 45</sup> The acid-amine complex pair formation keeps the pH value of the synthesis medium at 8-9, which is favorable for the growth of Fe<sub>3</sub>O<sub>4</sub> crystalline phase. The increase of oleic acid concentration can render a control over the pH from basic to acid condition. Therefore, we are having an increasing trend in particle size with the increase of OA concentration. At the OAm to OA mole ratio 6:5, the enhanced deprotonation of OA molecules and their highest electron-donating ability lead the preferential binding with cations on the specific Fe<sub>3</sub>O<sub>4</sub> facets and result in anisotropic nanoparticles. A further increase of the oleic acid concentration (OAm to OA mole ratio 6:7) facilitates the formation of acid-amine complex in the medium with leaving a less amount of oleylamine available in the medium for reducing the Fe-precursor. Hence resulted in a viscous brown color product of amorphous in nature (ESI, Fig. S1b). This argument is in concurrence with the molecular mechanic modeling results of Walt et. al.<sup>44</sup> Fig. 1g and 1h shows the TEM images of 24 and 28 nm sized MNPs produced by injecting the oleylamine at 200 °C and increasing the Fe(acac)<sub>3</sub> concentration as 20 and 30 mmol respectively. When oleic acid and Fe(acac)<sub>3</sub> mixture was heated to 200 °C without having OAm in the medium, they will form dimer and some will form a coordination bond with Fe-precursor. Then addition of oleylamine at 200 °C will slow the reaction and there will be

sufficient time for growth of the particles. The dimers will break and proton will react with oleylamine and results bigger sized nanoparticles. The XRD experiments are performed to determine the phase purity and the average crystallite size of the as-synthesized magnetic nanoparticles. The XRD analysis (Fig. S2, ESI) confirms that all samples are spinel magnetite ( $\text{Fe}_3\text{O}_4$ , ICCD card no. 79-0418). In the XRD pattern of 3 nm sized sample, a shoulder peak on the right of the (311) reflection is observed. We assign this shoulder to the existence of maghemite phase, which is a defect spinel polymorph usually seen in ultra-small sized iron oxide nanoparticles.<sup>46</sup> The particle size estimated using Scherrer's formula is consistent with the TEM analysis (Table S1, ESI). The calculated lattice constant increases from 8.37 Å to 8.39 Å with increase of the MNPs size from 3-32 nm (Table S1, ESI). The lattice constants of  $\text{Fe}_3\text{O}_4$  and  $\gamma\text{-Fe}_2\text{O}_3$  are 8.39 Å (ICCD card no. 79-0418) and 8.35 Å (ICCD card no. 39-1346) respectively, which confirms the pure magnetite phase of all the nanoparticles except the 3 nm sized MNPs.

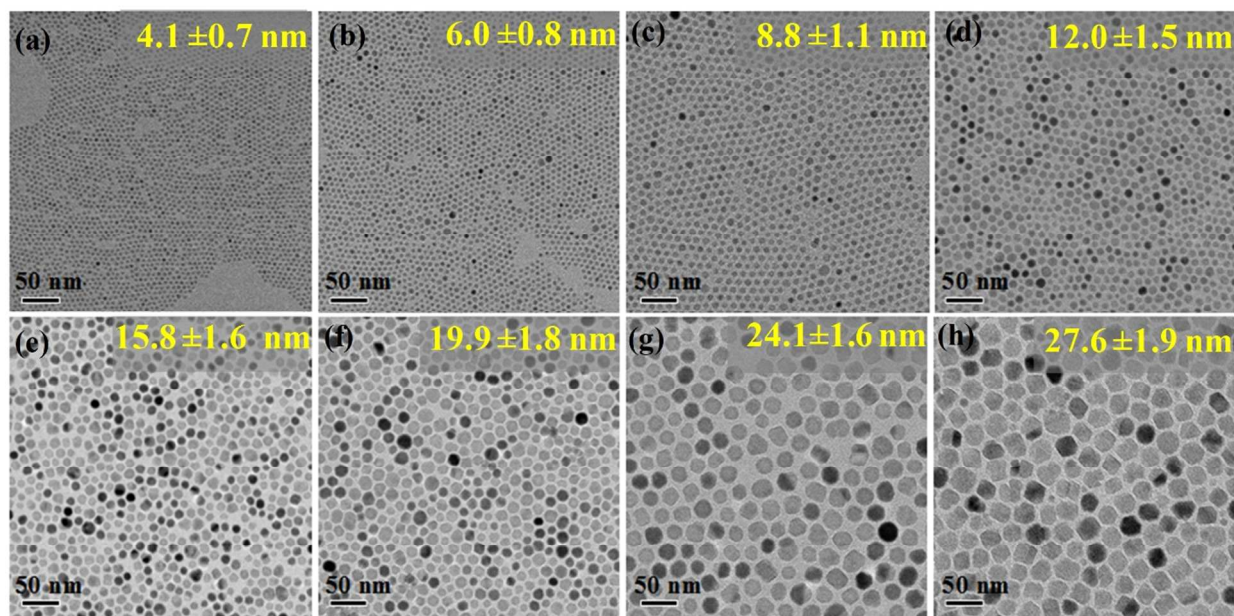


**Fig. 1.** TEM images of OA/OAm coated-  $\text{Fe}_3\text{O}_4$  nanoparticles synthesized with manipulation of Fe-precursor to OAm and OA mole ratio (Fe-precursor: OAm: OA) as (a) 1:7:0, (b) 1:5:0, (c) 1:3:0 (d) 2:6:1, (e) 2:6:2, (f) 2:6:3, (g) 2:6:3 and (h) 3 :6:3. In 24-28 nm sized MNP case, the

OAm was injected into the reaction medium at 200 °C. The particle size distribution histograms are given in Fig. S3 (ESI).

To further confirm the oxidation state of Fe in the prepared nanoparticles, the room temperature  $^{57}\text{Fe}$  Mössbauer spectroscopy was measured. Fig. 2 shows the Mössbauer spectra of 4, 16 and 28 nm  $\text{Fe}_3\text{O}_4$  nanoparticles. The experimental spectra are convoluted into two resolved sextets. The outer sextet A attributed to  $\text{Fe}^{3+}$  in the tetrahedral site and the inner sextet B to Fe ions located in the octahedral site of spinel magnetite. A clear presence of a singlet in the 4 nm  $\text{Fe}_3\text{O}_4$  nanoparticles denotes a part of Fe atoms may be in the superparamagnetic or nonmagnetic state, which indicates that the particles are non-stoichiometric<sup>47-50</sup> The computed hyperfine parameters: isomer shift, quadrupole moment and hyperfine fields are listed in Table S2 (ESI). The observed isomer shift and hyperfine fields values are comparable to the bulk, which affirms the MNPs are the pure  $\text{Fe}_3\text{O}_4$  phase.<sup>51</sup> The isomer shift in 4 nm  $\text{Fe}_3\text{O}_4$  nanoparticles has less value as compared to 16 nm and 28 nm size  $\text{Fe}_3\text{O}_4$  nanoparticles, which depicts that the content of  $\text{Fe}^{3+}$  ions is higher in the former case, revealing a better stoichiometry in 16 and 28 nm  $\text{Fe}_3\text{O}_4$  nanoparticles.<sup>52</sup> The quadrupole splitting value is almost zero for all the samples, which represents the cubic crystal structure of the MNPs

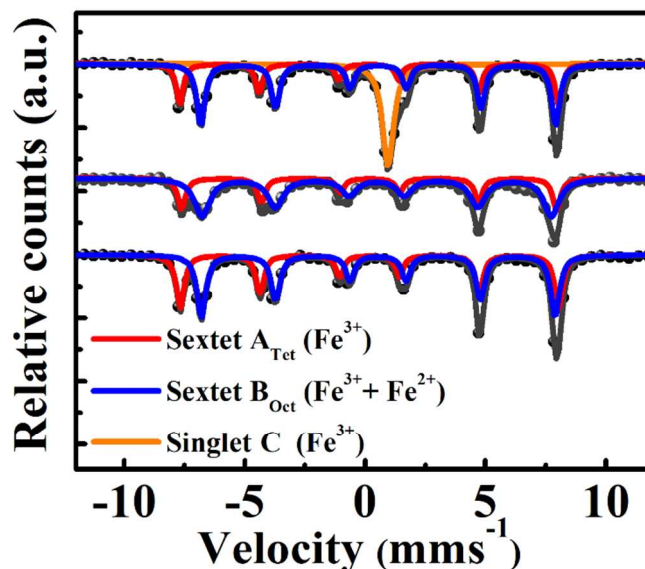


**Fig. 2.** Room temperature Mössbauer spectra of (i) 4 nm, (ii) 16 nm and (iii) 28 nm  $\text{Fe}_3\text{O}_4$  nanoparticles. The gray dots represent the experimental data and the black solid lines the fitted spectra. The experimental spectra fitted with two resolved sextets attributed to  $\text{Fe}^{3+}$  in the A site (red),  $\text{Fe}^{3+} + \text{Fe}^{2+}$  in the B site (blue) and singlet C is attributed to the shorter spin relaxation time of Fe.

The ZFC magnetization curve of the  $\text{Fe}_3\text{O}_4$  nanoparticles (3-24 nm) is shown in Fig. 3a. The temperature at the maximum of the ZFC magnetization curve is proportional to the average blocking temperature of the particles. Fig. 3a indicates that the average blocking temperature ( $T_B$ ) increases with the increase of the MNPs size (ESI, Fig. S4). The average value of  $T_B$ , was determined by taking the derivative of the difference of the ZFC and FC magnetization curve with respect to temperature i.e.,  $d[M_{ZFC} - M_{FC}]/dT$ . The  $T_B$  value is seen to increase linearly from 41 to 330 K (Fig. 3b) when the MNPs size increases from 3 to 24 nm. The effective anisotropy constant calculated using the Néel law ( $T_B = K_{\text{eff}}V/25k_B$ , where  $k_B$  and  $K_{\text{eff}}$  are the Boltzmann constant and the effective anisotropy constant, respectively<sup>33</sup>) decreased from  $1.1 \times 10^6$  to  $1.5 \times$

$10^4 \text{ J/m}^3$  (ESI, Fig. S5) with the increase of the MNPs size (bulk magnetite,  $1.35 \times 10^4 \text{ J/m}^3$ ).<sup>53</sup> The anisotropy constant includes the contributions from magnetocrystalline anisotropy and surface anisotropy. The surface effect (structure defects, broken symmetry bonds, strain and etc.) is prominent in ultra-small sized MNPs case and decreases with the particles size. In 16, 20 and 24 nm sized  $\text{Fe}_3\text{O}_4$  nanoparticles case a sharp drop in ZFC magnetization is observed at 120 K. This is an indication of the Verwey transition of magnetite. Below the transition temperature, the magnetic easy axis switches from the  $\langle 111 \rangle$  to  $\langle 100 \rangle$  direction, which leads to the reduction of ZFC magnetization.<sup>41</sup> Moreover, for the MNPs of size above 24 nm, the blocking process is dominated by Verwey transition. The room temperature magnetization loop of various sized  $\text{Fe}_3\text{O}_4$  nanoparticles is shown in Fig. 3c. At room temperature, all the samples in the size range 3 to 16 nm show superparamagnetic behavior without magnetic coercivity and remanence. While 20, 24, 28 and 32 nm sized  $\text{Fe}_3\text{O}_4$  nanoparticles shows a small loop opening with relatively low coercivity  $H_C < 300 \text{ Oe}$  (Fig. S6, ESI). The saturation magnetization ( $M_S$  at 13 kOe) gradually increases from 46 to 86 emu/g with an increase in particle size from 3 to 32 nm (Fig. 3d). To determine the thickness of spin disorder layer ( $t$ ), the variation of  $M_S$  with MNP sizes is fitted with the equation  $M_S = M_{S(bulk)}[1-6t/d]$  (Fig. 3d), where  $d$  is the MNPs size and  $M_{S(bulk)}$  is 92 emu/g, the bulk saturation magnetization value of  $\text{Fe}_3\text{O}_4$ . The obtained spin disorder layer thickness is 0.3 nm. However, the surface spin disorder effect decreases with the size due to the decrease of the surface-to-volume ratio, and therefore, the  $M_S$  value approaches to the bulk value (92 emu/g) with the increase of the MNPs size.<sup>54</sup> Such a control over the  $M_S$ ,  $H_C$  and  $K_{eff}$  with respect to size is of great importance to optimize the heating performance of  $\text{Fe}_3\text{O}_4$  nanoparticles.

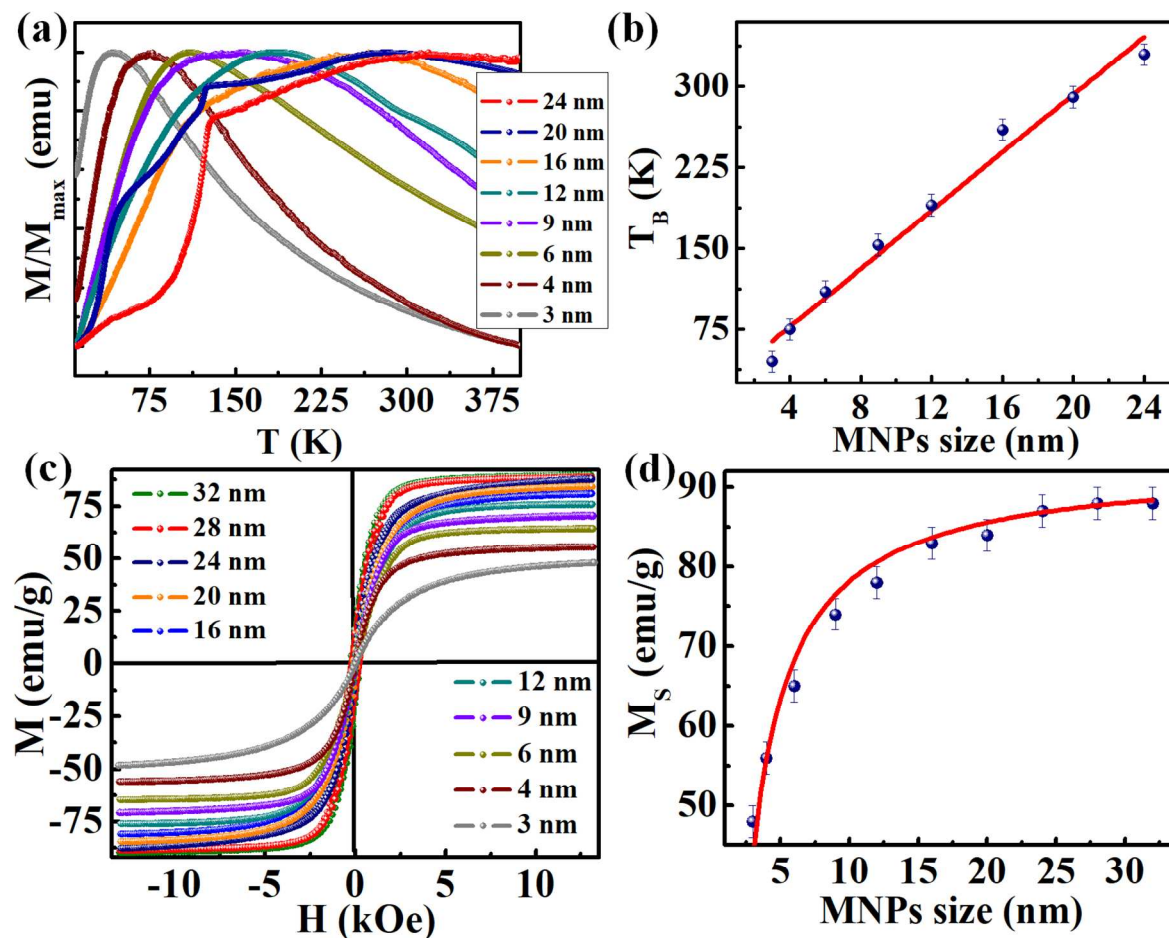


**Fig. 3.** (a) The ZFC magnetization plot for Fe<sub>3</sub>O<sub>4</sub> nanoparticles of different size. The ZFC measurement was done in a field of 50 Oe. (b) The blocking temperature ( $T_B$ ) vs. nanoparticle size plot shows a linear relationship between them. (c) Room temperature field-dependent magnetization curves of different sized Fe<sub>3</sub>O<sub>4</sub> nanoparticles. (d) Variation of the saturation magnetization as a function of MNPs size.

To prepare the stable aqueous dispersion, the as-prepared Fe<sub>3</sub>O<sub>4</sub> nanoparticles are subjected to surface modification with citric acid. The citric acid coating is confirmed from the Fourier transform infrared (FTIR) spectroscopy, dynamic light scattering (DLS) and  $\zeta$ -potential measurements. Fig. 4a shows a comparative analysis of the FTIR spectra of as-synthesized and citric acid functionalized 28 nm Fe<sub>3</sub>O<sub>4</sub> nanoparticles. In both the samples, the low-frequency

band at around  $572\text{ cm}^{-1}$  which corresponds to the Fe-O vibrational mode at octahedral and tetrahedral sites. The presence of Fe-O vibrational mode at  $572\text{ cm}^{-1}$  could be attributed to the magnetite phase of  $\text{Fe}_3\text{O}_4$ .<sup>41, 55</sup> In addition to  $572\text{ cm}^{-1}$ , two shoulder peaks are observed at around  $630$  and  $690\text{ cm}^{-1}$  are related to partial nanoparticles surface oxidation and/or vacancy ordering.<sup>41, 55</sup> In as prepared MNPs, the strong IR peak in the range of  $3760\text{ cm}^{-1}$  is assigned to the N-H stretching mode of primary amine, while the C-N stretching and  $\text{NH}_2$  scissoring bands appear at  $1032\text{ cm}^{-1}$  and  $1416\text{ cm}^{-1}$  respectively.<sup>56</sup> The peaks at  $1560\text{ cm}^{-1}$  are ascribed to the bidentate ( $-\text{COO}-\text{Fe}$ ) stretching mode of oleic acid binding, which matches well with the report by Barick et.al.<sup>57</sup> The bands at  $2845$  and  $2920\text{ cm}^{-1}$  are assigned to vibrations from  $\text{CH}_2$  groups in the long chain OAm and OA. In comparison with the as-synthesized sample, the citric acid- $\text{Fe}_3\text{O}_4$  samples show strong IR peaks of the symmetric stretching of  $\text{COO}^-$  ( $1390\text{ cm}^{-1}$ ), symmetric stretching of C-O ( $1606\text{ cm}^{-1}$ ), and C-OH stretching ( $1046\text{ cm}^{-1}$ ) group of citric acid which corroborates the presence of citric acid on the surface of  $\text{Fe}_3\text{O}_4$  nanoparticles. Further, the negative zeta potential values in the pH range 3-9 (Fig. 4b) also supports the presence of the citric acid groups at the MNPs surface. The observed negative zeta potential at high pH is probably due to the presence of negatively charged carboxylate ions on the surface of the MNPs. The citric acid- $\text{Fe}_3\text{O}_4$  nanoparticles are very stable as water colloids for about six months and no aggregation is observed (inset of Fig. 4b). There is no precipitation in water over a wide pH range (pH adjusted between 3– 9 by using HCl or NaOH). Further, the zeta potential of the aqueous dispersion 3-28 nm citric acid- $\text{Fe}_3\text{O}_4$  nanoparticles lies in the range of -22 to -30 eV (Fig. S7, ESI) which also indicated the aqueous stability for 3-28 nm size. Moreover, TEM micrographs show no change in size and shape after the ligand exchange with citric acid at a temperature of  $80\text{ }^\circ\text{C}$  (Fig. S8, ESI). The hydrodynamic diameters of the citric acid

functionalized  $\text{Fe}_3\text{O}_4$  nanoparticles are measured by dynamic light scattering (DLS: Fig. S9 a-f, ESI). The average hydrodynamic diameter of the citric acid-  $\text{Fe}_3\text{O}_4$  nanoparticles increases from 18 nm to 49 nm with the increase of the average TEM size from 4 to 28 nm. The mean hydrodynamic diameters are larger than the size obtained from TEM, due to the presence of associated and hydrated long chain citric acid layers. The saturation magnetization of the citric acid coated MNPs are 2-7 emu/g less than that of the as-synthesized  $\text{Fe}_3\text{O}_4$  nanoparticles (Table S3, ESI). The lower value of the saturation magnetization could be due to partial surface oxidation and also possibly due to the increased amount of the organic moieties on the surface of  $\text{Fe}_3\text{O}_4$  nanoparticles.

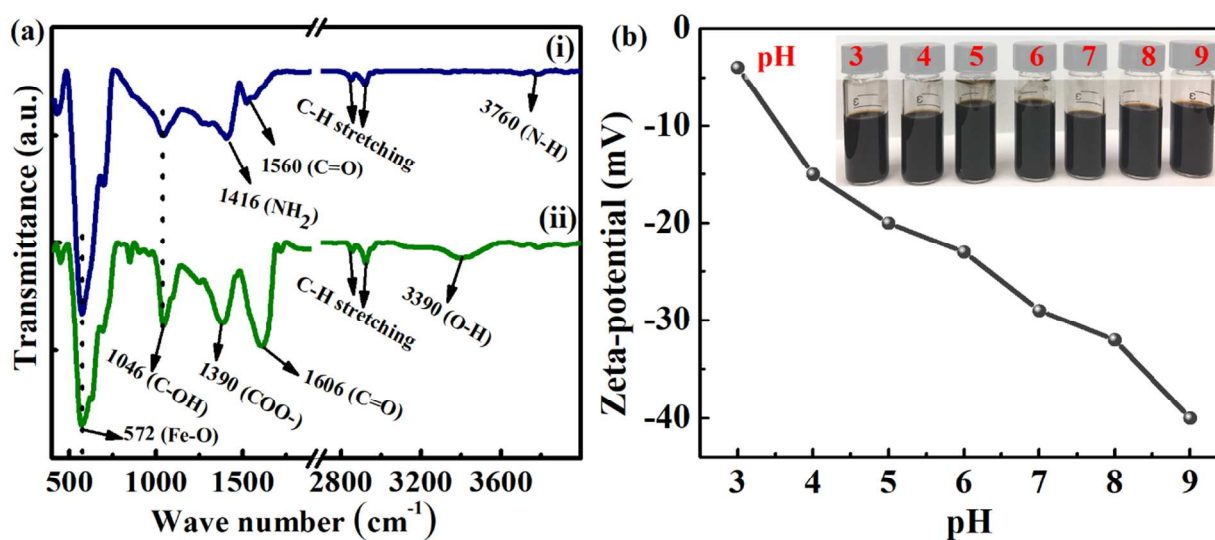


**Fig. 4:** (a) Comparative analysis of the FTIR spectra of: (i) as prepared  $\text{Fe}_3\text{O}_4$  and (ii) citric acid modified  $\text{Fe}_3\text{O}_4$  nanoparticles of average size 28 nm. (b) Zeta potential at different pH values of citric acid functionalized  $\text{Fe}_3\text{O}_4$  nanoparticles of average size 28 nm and the inset shows the photo of the aqueous suspension of  $\text{Fe}_3\text{O}_4$  nanoparticles after six months at different pH conditions.

The heating performance of the  $\text{Fe}_3\text{O}_4$  nanoparticles aqueous suspension was measured under an applied ACMF of 184, 234, 491 and 625 Oe at a fixed frequency of 265 kHz. The initial temperature of the MNPs suspension was set to a room temperature of 27 °C and then exposed to the ACMF for 1200 s. Fig. 5a represents the temperature variation as a function of measuring time for 3-32 nm sized  $\text{Fe}_3\text{O}_4$  MNPs with an ACMF 625 Oe. The SAR values calculated based on the initial temperature rise are shown in Fig. 5b. The SAR increases with the increase of the particle size and attains a maximum at a particle size of 28 nm, then the value decreases with further increase of the particle size. Interestingly, the increasing trend of the SAR has two different scenarios with respect to the MNPs size. The SAR value increases from 27-298 W/g of  $\text{Fe}_3\text{O}_4$  with the increases of MNPs size from 3-16 nm and with further increase of the MNPs size it increases rapidly. From  $M(T)$  and  $M(H)$  data we have seen a superparamagnetic behavior in 3-16 nm sized MNPs. According to the linear response theory (LRT), in the superparamagnetic regime the induction heating is mainly governed by the susceptibility loss determined by two size-dependent processes, Neel relaxation and rotational Brownian motion.<sup>12,</sup>  
<sup>58</sup> The susceptibility loss increases with the increase of the particle size due to the enhancement of MNPs magnetization and the anisotropy constant ( $K_{eff}$ ). Moreover, the higher  $K_{eff}$  can also lead to a resonance condition with maximum heating efficiency. In 3-16 nm MNPs case, the susceptibility is increased nearly three-fold with the size. Therefore, in superparamagnetic regime, the SAR values increase with the MNPs size. Above the 16 nm, increasing the MNPs size can suppress the susceptibility loss due to the particle moment blocking, and consequently the SAR should reduce. Several experimental studies on the size-dependent heating activity by MNPs reported that the maximum SAR value was achieved with MNPs of 12-15 nm, while SAR decreased rapidly as the size either increased or decreased (Table S4, ESI).<sup>26-30</sup> However, in our

case the SAR value increases sharply from 298 to 801 W/g with the increase of MNPs size from 16-28 nm. The fast increase of the SAR (above 16 nm) values could be due to the combined effect of susceptibility loss and hysteresis loss. In the ferromagnetic regime, the amount of dissipated heat is proportional to the area of the hysteresis loop.<sup>18, 58, 59</sup> Thus, the SAR values can be further optimized by contributions from the hysteresis loop. A similar observation reported by Jeun et. al. suggests that the SAR value in ferromagnetic regime increased with the MNPs size due to additional contribution of hysteresis loss.<sup>60</sup> Tong et.al also presented an increasing trend in the SAR values with the increase of MNPs from 5.6 nm to 40 nm. In particular, the 40 nm ferromagnetic nanoparticles have an SAR value approaching the theoretical limit under a clinically relevant ACMF. However, in our case the 32 nm sized MNPs showed a reduction in the heating efficiency. The decrease of the SAR value above 28 nm is attributed to the aggregation of the particles due to their higher magnetic moment. A partial aggregation in the MNPs dispersion is seen for the 32 nm sized MNPs during the hyperthermia measurement. With the increase of the ACMF amplitude the aggregation effect may be prominent and hence the SAR value decreases with the increase of the field strength. The agglomeration issue can be avoided by encapsulating the MNPs with biotinylated-phospholipid, PEG or Peptide to the hydrocarbon layer of the MNPs. The encapsulation can give a robust double-layer structure over the particle surface with the inner layer being the original oleate/oleylamine and the outer layer being hydrophilic functional group. The decrease of the SAR value above 28 nm size MNPs could also be possible due to dipolar interactions. The dipolar interaction effect can be prominent due to the large volume ( $V$ ), and saturation magnetization ( $M_S$ ). A concentration-dependent SAR value measurement for different sized MNPs (Fig. S10, ESI) further illustrated the role of dipolar interactions in ferromagnetic nanoparticles. In superparamagnetic MNPs case (12 and 16 nm

size), the SAR value linearly increases with the increase of the concentration from 1 mg to 4 mg, while the 24 and 28 nm sized MNPs exhibit a nonlinear feature. The non-linear trend, i.e. the slow increase of the SAR value in higher MNPs concentration (4mg/ml) possibly due to the collective-particle scenario, in which the system response is determined by the strong dipolar interactions. Conde-Leboran et al. have shown that with increasing strength of dipolar interactions, the effective anisotropy increases and the AC hysteresis loops area tend to become smaller, which is effectively lowered the SAR values.<sup>59</sup>

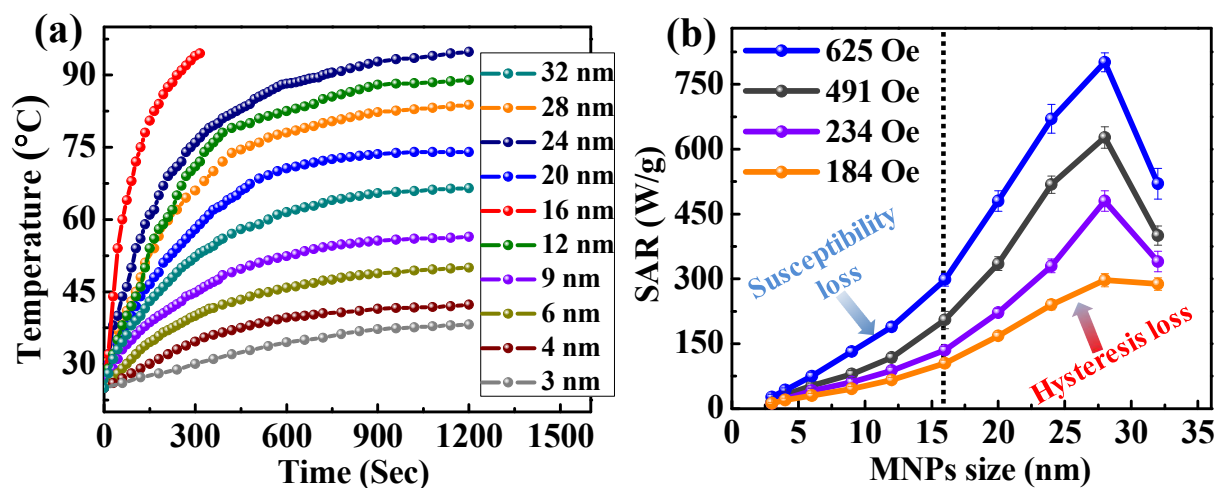


**Fig. 5.** (a) Temperature variation as a function of time for aqueous suspension (2 mg/ml) of  $\text{Fe}_3\text{O}_4$  MNPs (3-32 nm) under the ACMF (625 Oe) and (b) variation of the SAR values as a function of MNP size for different ACMF field (184-625 Oe).

To get a better insight into the hyperthermia heating mechanism, the temperature dependence of the in-phase ( $\chi'(T, f)$ ) and the out-of-phase ( $\chi''(T, f)$ ) components of the AC magnetic susceptibility for  $\text{Fe}_3\text{O}_4$  nanoparticles were measured. We found that the peak value of  $\chi'(T, f)$  and  $\chi''(T, f)$  and the corresponding blocking temperatures ( $T_m$ ) increased when the size of the  $\text{Fe}_3\text{O}_4$  nanoparticles increases from 3-16 nm (Fig. S11, ESI). Above 16 nm size, the

nanoparticles did not show recognizable peaks and the observed  $\chi''(T, f)$  amplitude also decreased because the AC field (5 Oe) was smaller than the coercive field of the large nanoparticles. The variation of  $T_m$  with  $\ln(\tau)$  is fitted with Vogel-Fulcher equation (Fig. S11d, ESI).<sup>54</sup> The anisotropy constant obtained from the best fitting decreased from  $7.1 \times 10^5$  to  $1.4 \times 10^4$  J/m<sup>3</sup> with the increase of Fe<sub>3</sub>O<sub>4</sub> size from 3-16 nm and is in good agreement with the values obtained from ZFC magnetization data. Both the ZFC magnetization and the AC susceptibility measurements indicate that the anisotropy constant of large Fe<sub>3</sub>O<sub>4</sub> nanoparticles (> 16 nm) approaches that of bulk magnetite ( $1.35 \times 10^4$  J/m<sup>3</sup>), which is dominated by the magnetocrystalline anisotropy. Thus, the bulk value of anisotropy constant can be used to calculate Neel relaxation time of the large-sized nanoparticles. Fig. 6a shows the size dependence of the Neel and the Brownian relaxation time for Fe<sub>3</sub>O<sub>4</sub> nanoparticles. The 3-16 nm Fe<sub>3</sub>O<sub>4</sub> nanoparticles show a dominate Neel relaxation ( $\tau_N$ ) whereas above 16 nm the Brownian relaxation ( $\tau_B$ ) has a significant contribution to the total relaxation time ( $\tau$ ). At low-amplitude fields, the relationship between power dissipation ( $P$ ) and Néel-Brown relaxation time is given,<sup>12,</sup>

61

$$P_{LRT} = \pi\mu_0\chi_0 H_0^2 f \frac{2\pi f\tau}{1+(2\pi f\tau)^2} \quad (1)$$

with  $\chi_0$  is the equilibrium susceptibility,  $H_0$  the ACMF amplitude,  $f$  the field frequency and  $\tau$  the Néel-Brown relaxation time, written as

$$\tau_B = \frac{3\eta V_H}{k_B T} \quad (2)$$

$$\tau_N = \frac{M_S}{2\gamma_0 K_{eff}^{3/2}} \left( \frac{\pi k_B T}{V} \right)^{1/2} \exp\left( \frac{K_{eff} V}{k_B T} \right) \quad (3)$$

Where  $\eta$  is the viscosity coefficient of the matrix fluid,  $k_B$  is the Boltzmann constant,  $T$  is the absolute temperature,  $V_H$  is the hydrodynamic volume and  $K_{eff}$  is the effective anisotropy constant. Because the Brownian and Néel processes take place in parallel, the effective relaxation time  $\tau$  is given by

$$\frac{1}{\tau} = \frac{1}{\tau_B} + \frac{1}{\tau_N} \quad (4)$$

In superparamagnetic regime ( $< 16$  nm), the Brownian contribution can be neglected,  $\tau = \tau_N$ .

From equation 1 and 3 it is clear that the maximum power loss is directly related to the  $\chi_0$  (amplitude of  $\chi''(T, f)$ ) and  $\tau_N$ . Further, a maximum heating efficiency can be achieved at the resonance condition, when the nanoparticles relax with the frequency of the ACMF ( $\tau \sim 1/2\pi f$ ).<sup>62</sup> In our case, the 16 nm and 12 nm Fe<sub>3</sub>O<sub>4</sub> nanoparticles have the reasonable  $\chi''(T, f)$  amplitude and relaxation time close to the ACMF frequency. At lower  $\tau$  ( $\tau < 1/2\pi f$ ), power losses increase with  $\tau$ , in other words, increase with the increase of nanoparticles size from 3 to 16 nm. While  $\tau > 1/2\pi f$ , our SAR results contradict the LRT model, which states that the SAR values decrease with size. The comparison between LRT model prediction and our experimental measurements indicates that the LRT model is applicable only for Fe<sub>3</sub>O<sub>4</sub> nanoparticles  $\leq 16$  nm. The failure of the LRT model to explain the heating mechanism of larger size Fe<sub>3</sub>O<sub>4</sub> nanoparticles could be due to the ferromagnetic behavior of nanoparticles.

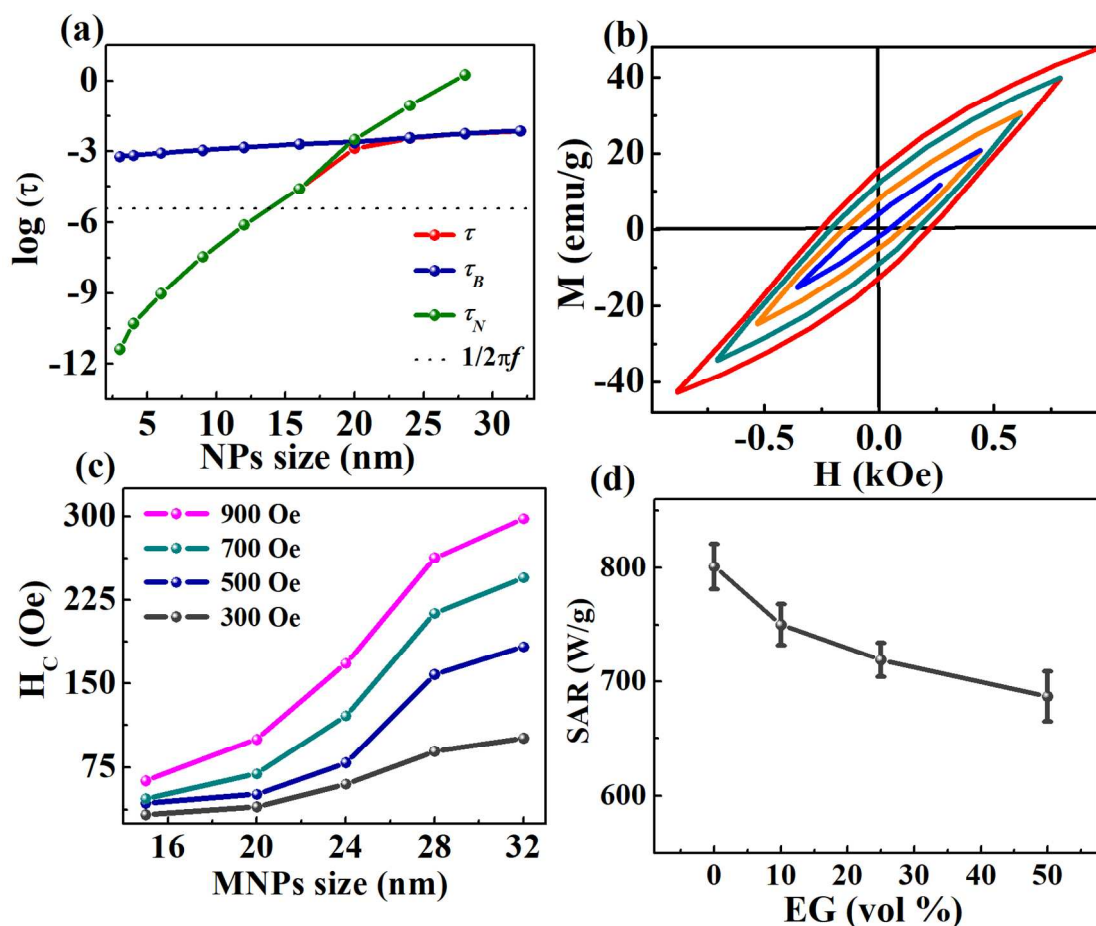


**Fig. 6.** (a) Neel relaxation time and Brownian relaxation time calculated using parameters derived from AC susceptibility measurements and hydrodynamic diameter, respectively. (b) Room temperature minor M–H loop of 28 nm MNPs at the maximum magnetic field of 300 (blue), 500 (orange), 700 (green) and 900 Oe (red), respectively. (c) Coercive field as a function of MNP size with the variation of the applied magnetic field. (d) The SAR values with increasing concentration of ethylene glycol (EG) in water.

In order to understand the contribution of hysteresis loss, the minor hysteresis loops for 6–28 nm sized MNPs in the range field 0–800 Oe was measured using the alternating gradient

magnetometer (AGM) (Fig. S12, ESI). Based on Stoner-Wohlfarth model, the amount of heat generated by the randomly oriented MNPs in one cycle is<sup>63</sup>,

$$P_{hys} = 2\mu_0 H_C M_S \quad (5)$$

As can be observed in Fig. 6b, at low fields, the shape of the loop looks like Rayleigh loops and the hysteresis loop area is small.<sup>58</sup> However, when the field keeps increasing, the hysteresis loop area rapidly increases (Fig. 6c). Compared to 16 nm sized, the hysteresis loop area of 28 nm is higher (See in Fig. 6c). Moreover, with the increase of the MNPs size the hysteresis loop area also increases. The improvement of the hysteresis loop area results in the enhanced hysteresis loss in the larger sized MNPs. Hence the SAR values increase sharply after 16 nm (Fig. 5b). In contrast to the superparamagnetic regime (3-16 nm), the SAR values for ferromagnetic nanoparticles are enhanced strongly with the increase of ACMF amplitude. For example, in 16 nm sized MNPs case the SAR value increases from 105 to 298 W/g (increased by 194 W/g) with the increase of ACMF amplitude from 184 to 625 Oe. Whereas in 28 nm sized MNPs, the SAR value enhanced by 504 W/g (from 297 to 801 W/g). The strong enhancement of the SAR value with the rise of ACMF amplitude is a typical behavior of nanoparticles in the ferromagnetic regime with the anisotropy axis aligned along the magnetic field direction. The square shape and saturated behavior of the hysteresis loop improve with the increase of the ACMF amplitude and lead to a rapid increase of SAR value. In ferromagnetic regime, we cannot rule out the contribution of susceptibility loss due to the Brownian rotation of MNPs. To suppress the physical rotation contribution, 10-50 % (in volume) of ethylene glycol (EG) was added to the aqueous dispersion of 28 nm Fe<sub>3</sub>O<sub>4</sub> nanoparticles. It can be seen from Fig. 6d, the SAR value decreased from 801 to 687 W/g with an increase of EG concentration 0-50 %. The synergistic contribution of hysteresis loss and susceptibility loss due to the Brownian rotation is responsible

for enhanced heating ability in 16-28 nm  $\text{Fe}_3\text{O}_4$  nanoparticles. The obtained highest SAR value for the 28 nm MNPs is an order higher than that of the commercially available nanoparticles, i.e. Ferumoxytol, Nanomag® D-SPIO, and Feridex (SAR > 100 W/g of Fe).<sup>64,65</sup> The experimental results clearly demonstrate a great importance of tuning the magnetic properties by nano-scaling laws to optimize the heating efficiency. In addition, it has been seen that the contribution of the hysteresis loss of the ferromagnetic  $\text{Fe}_3\text{O}_4$  nanoparticles to the heating efficiency is considerable and hence can be promising for *in vivo* applications.

#### 4. Conclusion

Monodispersed  $\text{Fe}_3\text{O}_4$  nanoparticles of mean size 3-32 nm have been successfully synthesized in gram quantities using oleic acid and oleylamine as the solvent, surfactant and the reducing agent. A systematic study of the size dependence of magnetic and inductive heating properties reveals that the larger sized  $\text{Fe}_3\text{O}_4$  nanoparticles (>16 nm) are in ferromagnetic regime ( $H_C < 300$  Oe), pure magnetite in phase, possessing bulk value of  $M_S$  (86 emu/g) and most importantly having extremely high SAR values. Further, the SAR values for ferromagnetic nanoparticles are enhanced strongly with the increase of ACMF amplitude than the superparamagnetic nanoparticles (3-16 nm) due to the increase of the hysteresis loss. The SAR value of 28 nm-sized  $\text{Fe}_3\text{O}_4$  nanoparticle suspension (801 W/g) is nearly one order higher than that of the commercially available ferrofluid. Contrary to the widely accepted the LRT model predictions, our experimental results claim that  $\text{Fe}_3\text{O}_4$  nanoparticles of size larger than 16 nm are more efficient for heating under the ACMF.

#### Acknowledgments

This work has been supported by the U.S. DoD/ARO under grant W911NF-11-1-0507, and the Center for Nanostructured Materials and Characterization Center for Materials and Biology at the University of Texas at Arlington.

## References

1. Y.-w. Jun, J.-w. Seo and J. Cheon, *Acc. Chem. Res.*, 2008, **41**, 179-189.
2. J.-H. Lee, Y.-M. Huh, Y.-w. Jun, J.-w. Seo, J.-t. Jang, H.-T. Song, S. Kim, E.-J. Cho, H.-G. Yoon and J.-S. Suh, *Nat. Med.*, 2006, **13**, 95-99.
3. K. Yan, P. Li, H. Zhu, Y. Zhou, J. Ding, J. Shen, Z. Li, Z. Xu and P. K. Chu, *RSC Adv.*, 2013, **3**, 10598-10618.
4. S. Chandra, K. C. Barick and D. Bahadur, *Adv. Drug Delivery Rev.*, 2011, **63**, 1267-1281.
5. S. Chandra, S. Nigam and D. Bahadur, *J. Biomed. Nanotechnol.*, 2014, **10**, 32-49.
6. K. C. Barick, S. Singh, D. Bahadur, M. A. Lawande, D. P. Patkar and P. A. Hassan, *J. Colloid Interface Sci.*, 2014, **418**, 120-125.
7. W. J. Atkinson, I. A. Brezovich and D. P. Chakraborty, *IEEE Trans. Biomed. Eng.*, 1984, **BME-31**, 70-75.
8. K. Simeonidis, M. P. Morales, M. Marciello, M. Angelakeris, P. de La Presa, A. Lazaro-Carrillo, A. Tabero, A. Villanueva, O. Chubykalo-Fesenko and D. Serantes, *Sci. Rep.*, 2016, **6**.
9. J. W. Hubbard, F. Orange, M. J. F. Guinel, A. J. Guenther, J. M. Mabry, C. M. Sahagun and C. Rinaldi, *ACS Appl. Mater. Interfaces*, 2013, **5**, 11329-11335.
10. Y. Agzenai, J. Pozuelo, J. Sanz, I. Perez and J. Baselga, *Recent patents on nanotechnology*, 2015, **9**, 43-50.
11. D. Yoo, J.-H. Lee, T.-H. Shin and J. Cheon, *Acc. Chem. Res.*, 2011, **44**, 863-874.
12. R. E. Rosensweig, *J. Magn. Magn. Mater.*, 2002, **252**, 370-374.
13. X. L. Liu, H. M. Fan, J. B. Yi, Y. Yang, E. S. G. Choo, J. M. Xue, D. D. Fan and J. Ding, *J. Mater. Chem.*, 2012, **22**, 8235-8244.
14. D. Maity, P. Chandrasekharan, C.-T. Yang, K.-H. Chuang, B. Shuter, J.-M. Xue, J. Ding and S.-S. Feng, *Nanomedicine*, 2010, **5**, 1571-1584.
15. J.-H. Lee, J.-t. Jang, J.-s. Choi, S. H. Moon, S.-h. Noh, J.-w. Kim, J.-G. Kim, I.-S. Kim, K. I. Park and J. Cheon, *Nature Nanotech.*, 2011, **6**, 418-422.
16. Z. Nemat, J. Alonso, H. Khurshid, M. H. Phan and H. Srikanth, *RSC Adv.*, 2016, **6**, 38697-38702.
17. K. Vamvakidis, S. Mourdikoudis, A. Makridis, E. Paulidou, M. Angelakeris and C. Dendrinos-Samara, *J. Colloid Interface Sci.*, 2018, **511**, 101-109.
18. R. Das, J. Alonso, Z. Nemat, Porshokouh, V. Kalappattil, D. Torres, M.-H. Phan, E. Garaio, J. Á. García, J. L. Sanchez Llamazares and H. Srikanth, *J. Phys. Chem. C*, 2016, **120**, 10086-10093.
19. Y. Lv, Y. Yang, J. Fang, H. Zhang, E. Peng, X. Liu, W. Xiao and J. Ding, *RSC Adv.*, 2015, **5**, 76764-76771.
20. J. Kolosnjaj-Tabi, R. Di Corato, L. Lartigue, I. Marangon, P. Guardia, A. K. A. Silva, N. Luciani, O. Clément, P. Flaud, J. V. Singh, P. Decuzzi, T. Pellegrino, C. Wilhelm and F. Gazeau, *ACS Nano*, 2014, **8**, 4268-4283.

21. P. Guardia, R. Di Corato, L. Lartigue, C. Wilhelm, A. Espinosa, M. Garcia-Hernandez, F. Gazeau, L. Manna and T. Pellegrino, *ACS nano*, 2012, **6**, 3080-3091.
22. J. Mohapatra, A. Mitra, M. Aslam and D. Bahadur, *IEEE Trans. Magn.*, 2015, **51**, 1-3.
23. P. Hugounenq, M. Levy, D. Alloyear, L. Lartigue, E. Dubois, V. Cabuil, C. Ricolleau, S. Roux, C. Wilhelm, F. Gazeau and R. Bazzi, *J. Phys. Chem. C*, 2012, **116**, 15702-15712.
24. L. Lartigue, P. Hugounenq, D. Alloyear, S. P. Clarke, M. Lévy, J.-C. Bacri, R. Bazzi, D. F. Brougham, C. Wilhelm and F. Gazeau, *ACS Nano*, 2012, **6**, 10935-10949.
25. Z. Nemati, J. Alonso, L. Martinez, H. Khurshid, E. Garaio, J. Garcia, M. Phan and H. Srikanth, *J. Phys. Chem. C*, 2016, **120**, 8370-8379.
26. Y. Yamamoto, K. Horiuchi, M. Takeuchi, N. Tanaka, R. Aihara, N. Takeuchi and S. Fujita, *J. Appl. Phys.*, 2014, **116**, 123906.
27. M. Gonzales-Weimuller, M. Zeisberger and K. M. Krishnan, *J. Magn. Magn. Mater.*, 2009, **321**, 1947-1950.
28. E. Lima, T. E. Torres, L. M. Rossi, H. R. Rechenberg, T. S. Berquo, A. Ibarra, C. Marquina, M. R. Ibarra and G. F. Goya, *J. Nanopart. Res.*, 2013, **15**, 1654.
29. P. De la Presa, Y. Luengo, M. Multigner, R. Costo, M. Morales, G. Rivero and A. Hernando, *J. Phys. Chem. C*, 2012, **116**, 25602-25610.
30. M. Levy, A. Quarta, A. Espinosa, A. Figuerola, C. Wilhelm, M. García-Hernández, A. Genovese, A. Falqui, D. Alloyear and R. Buonsanti, *Chem. Mater.*, 2011, **23**, 4170-4180.
31. H. Khurshid, W. Li, S. Chandra, M.-H. Phan, G. C. Hadjipanayis, P. Mukherjee and H. Srikanth, *Nanoscale*, 2013, **5**, 7942-7952.
32. J.-H. Lee, Y.-M. Huh, Y.-w. Jun, J.-w. Seo, J.-t. Jang, H.-T. Song, S. Kim, E.-J. Cho, H.-G. Yoon, J.-S. Suh and J. Cheon, *Nat. Med.*, 2007, **13**, 95-99.
33. J. Mohapatra, A. Mitra, D. Bahadur and M. Aslam, *CrystEngComm*, 2013, **15**, 524-532.
34. J. Mohapatra, A. Mitra, H. Tyagi, D. Bahadur and M. Aslam, *Nanoscale*, 2015, **7**, 9174-9184.
35. J. Park, K. An, Y. Hwang, J.-G. Park, H.-J. Noh, J.-Y. Kim, J.-H. Park, N.-M. Hwang and T. Hyeon, *Nat. Mater.*, 2004, **3**, 891-895.
36. S. Sun and H. Zeng, *J. Am. Chem. Soc.*, 2002, **124**, 8204-8205.
37. S. Sun, H. Zeng, D. B. Robinson, S. Raoux, P. M. Rice, S. X. Wang and G. Li, *J. Am. Chem. Soc.*, 2004, **126**, 273-279.
38. H. M. Joshi, Y. P. Lin, M. Aslam, P. V. Prasad, E. A. Schultz-Sikma, R. Edelman, T. Meade and V. P. Dravid, *J. Phys. Chem. C*, 2009, **113**, 17761-17767.
39. M. Aslam, E. A. Schultz, T. Sun, T. Meade and V. P. Dravid, *Cryst. Growth Des.*, 2007, **7**, 471-475.
40. Z. Xu, C. Shen, Y. Hou, H. Gao and S. Sun, *Chem. Mater.*, 2009, **21**, 1778-1780.
41. A. Mitra, J. Mohapatra, S. S. Meena, C. V. Tomy and M. Aslam, *J. Phys. Chem. C*, 2014, **118**, 19356-19362.
42. E. C. Vreeland, J. Watt, G. B. Schober, B. G. Hance, M. J. Austin, A. D. Price, B. D. Fellows, T. C. Monson, N. S. Hudak, L. Maldonado-Camargo, A. C. Bohorquez, C. Rinaldi and D. L. Huber, *Chem. Mater.*, 2015, **27**, 6059-6066.
43. N. T. K. Thanh, N. Maclean and S. Mahiddine, *Chem. Rev.*, 2014, **114**, 7610-7630.
44. R. A. Harris, P. M. Shumbula and H. van der Walt, *Langmuir*, 2015, **31**, 3934-3943.
45. W. Bu, Z. Chen, F. Chen and J. Shi, *J. Phys. Chem. C*, 2009, **113**, 12176-12185.
46. L. M. Bronstein, X. Huang, J. Retrum, A. Schmucker, M. Pink, B. D. Stein and B. Dragnea, *Chem. Mater.*, 2007, **19**, 3624-3632.
47. G. Da Costa, E. De Grave, P. De Bakker and R. Vandenberghe, *Clays Clay Miner.*, 1995, **43**, 656-668.
48. E. De Grave, R. M. Persoons, R. E. Vandenberghe and P. M. A. de Bakker, *Phys. Rev. B*, 1993, **47**, 5881-5893.

49. F. K. Lotgering and A. M. V. Diepen, *J. Phys. Chem. Solids*, 1977, **38**, 565-572.
50. A. H. Morrish, K. Haneda and P. Schurer, *J. Journal de Physique*, 1976, **37**, C6-301-C306-305.
51. J. Daniels and A. Rosencwaig, *J. Phys. Chem. Solids*, 1969, **30**, 1561-1571.
52. H. Topsøe, J. Dumesic and M. Boudart, *J. Phys. Colloquia*, 1974, **35**, C6-411-C416-413.
53. A. Demortiere, P. Panissod, B. P. Pichon, G. Pourroy, D. Guillon, B. Donnio and S. Begin-Colin, *Nanoscale*, 2011, **3**, 225-232.
54. J. Mohapatra, A. Mitra, D. Bahadur and M. Aslam, *J. Alloys Compd.*, 2015, **628**, 416-423.
55. T. J. Daou, J. M. Grenèche, G. Pourroy, S. Buathong, A. Derory, C. Ulhaq-Bouillet, B. Donnio, D. Guillon and S. Begin-Colin, *Chem. Mater.*, 2008, **20**, 5869-5875.
56. M. Chen, Y.-G. Feng, X. Wang, T.-C. Li, J.-Y. Zhang and D.-J. Qian, *Langmuir*, 2007, **23**, 5296-5304.
57. S. Nigam, K. C. Barick and D. Bahadur, *J. Magn. Magn. Mater.*, 2011, **323**, 237-243.
58. S. Ruta, R. Chantrell and O. Hovorka, *Sci. Rep.*, 2015, **5**, 9090.
59. I. Conde-Leboran, D. Baldomir, C. Martinez-Boubeta, O. Chubykalo-Fesenko, M. del Puerto Morales, G. Salas, D. Cabrera, J. Camarero, F. J. Teran and D. Serantes, *J. Phys. Chem. C*, 2015, **119**, 15698-15706.
60. M. Jeun, S. Lee, J. Kyeong Kang, A. Tomitaka, K. Wook Kang, Y. Il Kim, Y. Takemura, K.-W. Chung, J. Kwak and S. Bae, *Appl. Phys. Lett.*, 2012, **100**, 092406.
61. J. Carrey, B. Mehdaoui and M. Respaud, *J. Appl. Phys.*, 2011, **109**, 083921-083917.
62. B. Mehdaoui, A. Meffre, J. Carrey, S. Lachaize, L. M. Lacroix, M. Gougeon, B. Chaudret and M. Respaud, *Adv. Funct. Mater.*, 2011, **21**, 4573-4581.
63. S. Tong, C. A. Quinto, L. Zhang, P. Mohindra and G. Bao, *ACS Nano*, 2017, **11 (7)**, 6808-6816.
64. J. P. Bullivant, S. Zhao, B. J. Willenberg, B. Kozissnik, C. D. Batich and J. Dobson, *Int. J. Mol. Sci.*, 2013, **14**, 17501-17510.
65. R.R. Shah, T.P. Davis, A.L. Glover, D.E. Nikles, C.S. Brazel, *J. Magn. Magn. Mater.*, 2015, **387**, 96-106.

## Graphical abstract

